

Microlensing of Central Images in Strong Gravitational Lens Systems

Gregory Dobler¹, Charles R. Keeton², & Joachim Wambsganss³

¹*Department of Physics and Astronomy, University of Pennsylvania, 209 S. 33rd Street, Philadelphia, PA 19104 USA*

²*Department of Physics and Astronomy, Rutgers University, 136 Frelinghuysen Road, Piscataway, NJ 08854 USA*

³*Astronomisches Rechen-Institut, Zentrum für Astronomie, Universität Heidelberg, Mönchhofstrasse 12-14, 69120 Heidelberg, Germany*

24 May 2019

ABSTRACT

We study microlensing of the faint images that form close to the centers of strong gravitational lens galaxies. These central images, which have finally begun to yield to observations, naturally appear in dense stellar fields and may be particularly sensitive to fine granularity in the mass distribution. Since central images are highly overfocussed (i.e., demagnified compared to an unlensed image), their microlensing magnification maps differ strikingly from the maps for normal, magnified images. The dispersion in microlensing magnifications is generally larger for central images than for normal bright images, especially when the source is comparable to or larger than the stellar Einstein radius. The dispersion depends in a complicated way on the fraction of the surface mass density contained in stars; that behavior may hold the key to using microlensing as a probe of the relative densities of stars and dark matter in the cores of distant galaxies. Quantitatively, we predict that the central image C in PMN J1632–0033 has a magnification dispersion of 0.23–0.25 dex for $R_{\text{src}}/R_{\text{E}} \lesssim 1$, or 0.11 dex for $R_{\text{src}}/R_{\text{E}} = 10$. For comparison, the dispersions are 0.19–0.23 dex for image B and 0.02–0.05 dex for image A, if $R_{\text{src}}/R_{\text{E}} \lesssim 1$; and just 0.04 dex for B and 0.003 dex for A if $R_{\text{src}}/R_{\text{E}} = 10$. (The dispersions can be extrapolated to larger source sizes as $\sigma \propto R_{\text{src}}^{-1}$.) Thus, central images are more susceptible than other lensed images to microlensing, but not in a way that will pose significant problems for astrophysical applications that rely on them.

Key words: galaxies — stellar populations — gravitational lensing

1 INTRODUCTION

Two aspects of strong gravitational lensing that date back 25 years have attracted much recent interest. Microlensing, or variations in the (optical) fluxes of lensed quasar images that are induced by individual stars in the lens galaxy, was first discussed by Chang & Refsdal (1979). The phenomenon has now been observed in several lens systems (Woźniak et al. 2000; Schechter et al. 2003; Richards et al. 2004). It can be used to learn about the stellar components (Gott 1981; Wambsganss 1990b; Pelt et al. 1998; Schmidt & Wambsganss 1998; Wyithe et al. 2000; Kochanek 2004) and the relative densities of stars and dark matter (Schechter & Wambsganss 2002, 2004) in lens galaxies, and to probe structure in the source quasars at stunning micro-arcsecond resolution (Grieger et al. 1988, 1991; Agol & Krolik 1999; Mineshige & Yonehara 1999; Fluke & Webster 1999; Goicoechea et al. 2004).

Central or “odd” lensed images were originally predicted by Dyer & Roeder (1980) and Burke (1981). If the

inner surface mass density of a lens galaxy is shallower than $\Sigma \propto R^{-1}$ and there is no point mass at the center, then lensing should always produce an odd number of images. Nearly all observed lenses, however, exhibit two or four images. The prediction and observations can be reconciled by noting that one of the expected images should be very close to the center of the lens galaxy and demagnified by the high central surface density there (e.g., Wallington & Narayan 1993; Norbury et al. 2000; Rusin & Ma 2001; Keeton 2003). That makes central images difficult to detect — and indeed the first ones have only just been found. Winn et al. (2003, 2004) detected a central image at radio wavelengths in the asymmetric 2-image lens PMN J1632–0033, while Inada et al. (2005) detected a central image at optical wavelengths in the unusual 4-image cluster lens SDSS J1004+4112.

Our goal in this paper is to combine the two phenomena and study microlensing of central, demagnified images. The issue is timely since central images are now being observed, and compelling since the images naturally form in regions where the density of stars is high and microlensing

arXiv:astro-ph/0507522v1 21 Jul 2005

Image	κ	γ	μ
A	0.370	0.422	4.570
B	3.309	2.859	0.352
C	16.517	13.796	0.020

Table 1. Total convergence κ , shear γ , and magnification μ for each of the three images in PMN J1632–0033, from spherical power law plus external shear lens models by Winn et al. (2003, 2004). “C” indicates the central, highly demagnified image.

seems inevitable. We perform “numerical experiments” in an attempt to identify and quantify the important microlensing effects, and to raise questions that may prompt further analytic study.

We customize our calculations to the lens PMN J1632–0033, because it is both a known central image system and also a prototype for the sorts of systems that are expected to yield the most central images in the future (Keeton 2003; Bowman et al. 2004). Winn et al. (2003, 2004) recently studied a wide range of mass models for PMN J1632–0033, which can be used to estimate the total convergence κ and shear γ at the positions of the images. The lens data, including the central image, are consistent with a simple power law surface mass density $\Sigma \propto R^{-\alpha}$ with $\alpha = 0.91 \pm 0.02$, plus a small external tidal shear. Table 1 gives the values of κ and γ for such a model, which we adopt as inputs for our microlensing simulations.

2 METHODS

We use standard methods for microlensing calculations. Specifically, we pick a patch around an image that is large compared with a stellar Einstein radius (the scale for microlensing), but small compared with the global scale of the lens so that the mean densities of stars and dark matter are essentially constant across the patch. Attaining this balance is not difficult, because the global scale is set by the $1''.5$ image separation, while the stellar Einstein radius is $R_E \sim 2(M/M_\odot)^{1/2} \times 10^{-6}$ arcsec. In practice, we typically consider a rectangular patch in the image plane chosen so that it maps into a square patch in the source plane that is $100R_E$ on a side (see below). Without loss of generality, we can choose a coordinate system aligned with the direction of the local shear. We assume that a fraction

$$f = \kappa_{\text{stars}} / \kappa_{\text{tot}} \quad (1)$$

of the total surface mass density (or convergence) is contributed by stars. We use that to determine the number of stars in the patch, and then distribute the stars randomly.

In this pilot study, we assume that all stars have the same mass, and we always work in units of the stellar Einstein radius R_E . Previous analyses have shown that the microlensing magnification distribution is at best weakly dependent on the distribution of stellar masses, at least for a point source.¹ That result must break down for a finite

source, which would be insensitive to stars below some mass threshold (roughly corresponding to $R_E \lesssim R_{\text{src}}$). The full problem — microlensing of a finite source by stars with unequal masses — is certainly interesting, but beyond the scope of this paper.

We use ray-shooting software by Wambsganss (1990a,b, 1999) to perform the microlensing simulations. Briefly, the software “shoots” a large number ($\gtrsim 10^8$) of light rays from the observer through the lens/image plane into the source plane, and collects them in small pixels. The magnification of a (point) source at a given position is proportional to the number of rays in the pixel at that position. The end product is a magnification map in the source plane. We can then obtain the magnification probability distribution by making a histogram of the pixel magnifications in the magnification map. To consider a source with a finite extent, all we need to do is convolve the magnification map with the surface brightness distribution of the source before making the histogram. For simplicity, we use a Gaussian source with half-light radius R_{src} , since Mortonson et al. (2004) argue that the detailed structure of the source hardly affects magnification distributions provided that the half-light radius is the same.

The physical input parameters for the simulations are the total convergence and shear, which we take from Table 1, and the fraction f of mass in stars, which we vary (see §3). The technical input parameters are the size of the magnification map and the number of pixels. We seek to consider sources both smaller and larger than R_E , and in particular find the range $0.1 \leq R_{\text{src}}/R_E \leq 10$ to be both interesting and tractable. In order to have many independent source positions in a given magnification map, we use maps that are $100R_E$ on a side. In order to have enough pixels to handle small sources, we use maps with 1024×1024 pixels.

We show typical magnification maps in Figure 1 (for $f = 100\%$ of the surface density in stars), with the caveat that to make the features visible we only show $(30R_E)^2$ maps here. The map for image C in particular shows that there is structure on scales of tens of Einstein radii, so even a $(100R_E)^2$ map does not contain a fully representative sample of magnifications. To obtain fair sampling, we create 50 independent magnification maps for each image, and compute the final magnification distributions from the combination of all of them. A fringe benefit of this approach is that we can consider the 50 magnifications maps to be independent realizations of the microlensing calculation, and use bootstrap or jackknife resampling (e.g., Efron 1982) to estimate the statistical uncertainties in our analysis.

3 RESULTS

The qualitative differences in the three magnification maps shown in Figure 1 are striking. For image A, which forms at a local minimum in the time delays surface and has relatively low values of the convergence and shear leading to a modest amplification, the map shows the familiar caustic network (e.g., Wambsganss 1990a; Schneider et al. 1992; Wambsganss 1999). The caustics are preferentially stretched

¹ The magnification distribution was long thought to be independent of the microlens mass function (Schneider 1987; Wambsganss 1992; Lewis & Irwin 1995; Wyithe & Turner 2001). However,

Schechter et al. (2004) recently presented results from numerical experiments suggesting that there is a weak dependence.

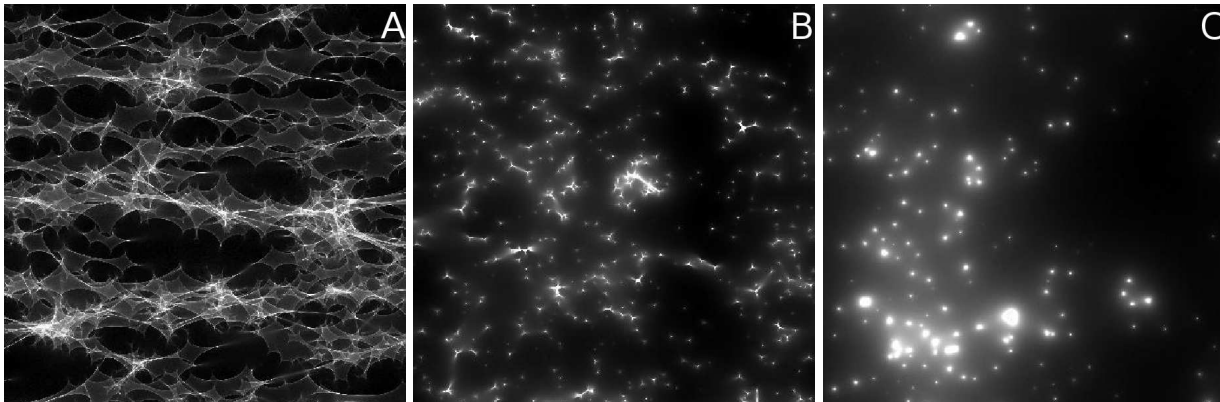


Figure 1. Sample magnification maps for images A, B, and C. The maps are $30R_E$ on a side, and the fraction of surface mass density in stars is $f = 100\%$.

along the horizontal axis because we have chosen coordinates aligned with the local shear. For image B, which forms at a saddle point in the time delay surface and is modestly demagnified, careful inspection reveals that the map shows many of the 3-pointed cusps that are characteristic of microlensing when the parity is negative (e.g., Schneider et al. 1992; Petters et al. 2001). These results are familiar. What is surprising is the map for image C, which forms at a local maximum in time delay surface and is highly demagnified. This map looks very different from the familiar, traditional caustics. It exhibits round, concentrated blobs of high magnification, surrounded by large regions of low magnification. As noted above, there is strong inhomogeneity even on scales of tens of Einstein radii. These features are known to occur for highly overfocussed (i.e., demagnified compared to an unlensed image) microlensing scenarios (e.g., Wambsganss 1990a; Schneider et al. 1992; Petters et al. 2001), but they have not been explored in much detail before.

The magnification distributions for different source sizes and different images are shown in Figure 2. In general, the distributions appear to be smooth and fairly symmetric in $\log \mu$. The exception is the case of image A with a small source ($R_{\text{src}}/R_E \lesssim 0.1$), whose magnification distribution shows three distinct peaks. The peaks can be understood in terms of the caustic network (e.g., Rauch et al. 1992; Granot et al. 2003): from low to high μ , the first peak corresponds to sources outside all caustics, the second peak to sources inside a single caustic (so there is one additional pair of microimages), and the third peak to sources inside a pair of overlapping caustics (so there are two extra pairs of microimages). In fact, there are higher-order peaks corresponding to source positions where more caustics overlap, but those peaks blur together and do not appear as clear features in the final magnification distribution (see Granot et al. 2003, especially their Fig. 4). The multi-peak structure disappears as the source size increases, because a large source ($R_{\text{src}}/R_E \gtrsim 1$) generally extends over one or more caustics, so the regions of different image multiplicity in the source plane are smeared out and disappear as distinct maxima in the magnification distribution. The same argument explains why the multi-peak structure is not seen at all for images B and C: for these images, the scale of struc-

tures in the magnification maps is smaller than the smallest source we consider (cf. Figure 1).

An important qualitative feature of the magnification distributions is that the width decreases as the source size increases. The width can be considered to represent either the likelihood that the magnification at any given time is different from what a smooth model would predict, or the RMS amplitude of variations in time. Thus, we may say that the larger the source, the less it is affected by microlensing — which makes intuitive sense. To quantify this effect, we compute the dispersion in $\log \mu$, namely

$$\sigma = [(\langle (\log \mu)^2 \rangle) - \langle \log \mu \rangle^2]^{1/2}, \quad (2)$$

where the average is over source positions. Figure 3 shows that the magnification dispersion σ falls monotonically as the source size increases (cf. Deguchi & Watson 1987; Refsdal & Stabell 1991, 1997). It remains relatively constant until the source size becomes comparable to the stellar Einstein radius, and then drops rapidly. At large source size, the dispersion decreases as $\sigma \propto R_{\text{src}}^{-1}$, as expected from previous simulations as well as analytic arguments (Refsdal & Stabell 1991, 1997). For $R_{\text{src}}/R_E \gtrsim 0.3$, the ordering of the images is independent of the source size: image C is most affected by microlensing, followed by image B, and finally image A. One curious result is that all three images have roughly the same magnification dispersion when the source is small ($R_{\text{src}}/R_E \lesssim 0.3$); we do not know whether this is a coincidence or reflects something more fundamental.

So far we have assumed that $f = 100\%$ of the surface mass density for each image is in stars, which is probably valid for image C but wrong for image A. The next step is to consider how the results change as we decrease f , as shown in Figure 4. For images A and B, the dispersion falls monotonically as f decreases. At first glance, the result for image B seems to contradict the finding by Schechter & Wambsganss (2002) that decreasing f can *increase* the magnification dispersion for saddle images. The difference is probably explained by the fact that Schechter & Wambsganss considered a highly magnified saddle image ($\mu = 9.5$), such as would be seen in a bright minimum/saddle pair straddling a critical curve in a 4-image lens; whereas our image B has a modest demagnification ($\mu = 0.35$), corresponding to a

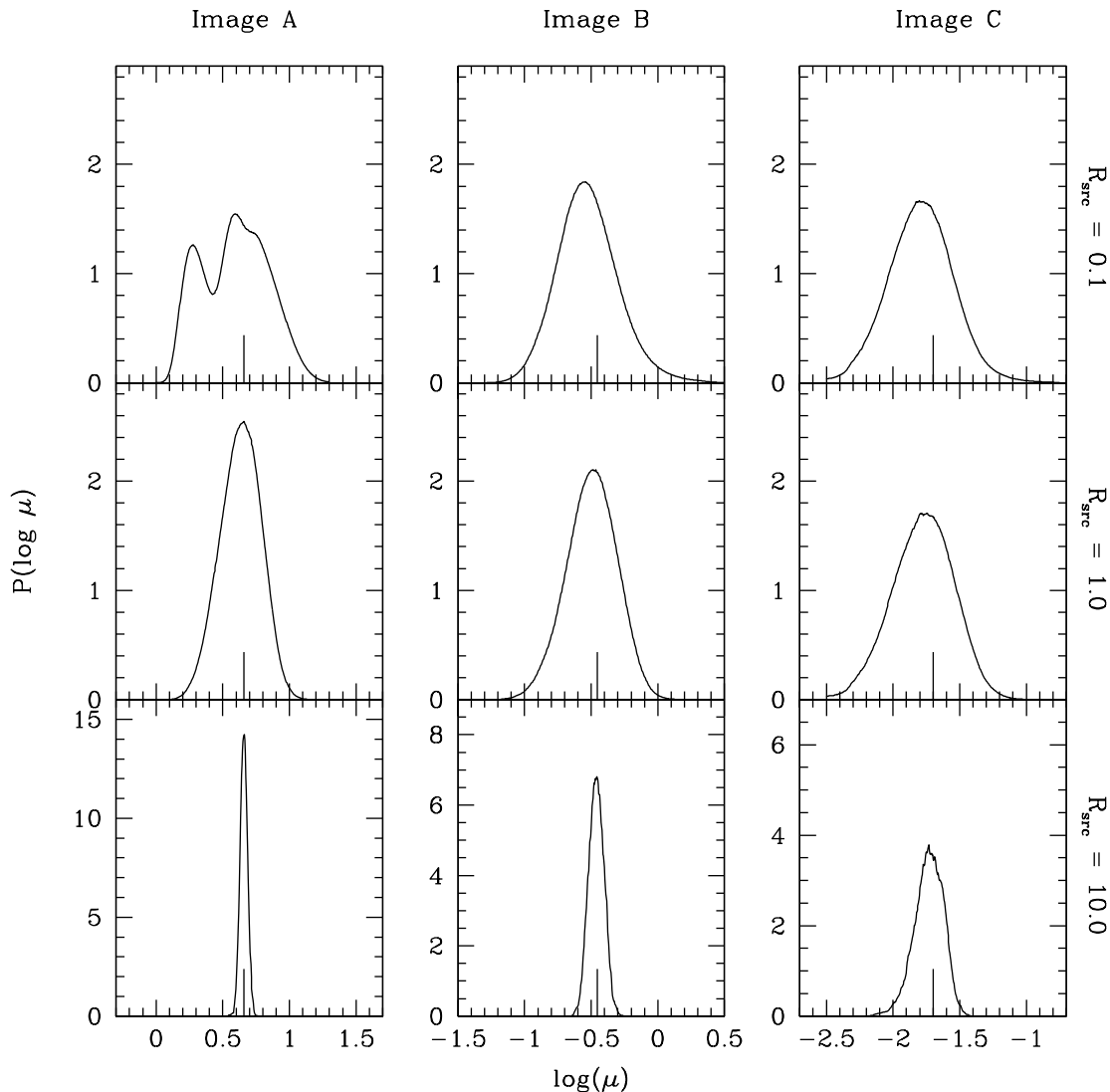


Figure 2. Magnification distributions for the three images (left to right), for three different source sizes (top to bottom), and $f = 100\%$ of the mass in stars. The source is modeled as a Gaussian with half-light radius R_{src} (quoted in units of R_E). The distributions for each image are derived from 50 independent realizations of $(100R_E)^2$ magnification maps. Each probability distribution $P(\log \mu)$ is normalized to unit area, but the vertical axis scale varies in the bottom panels. Any apparent jaggedness is numerical noise. The vertical bar marks $\log \mu_0$, where μ_0 is the magnification in the absence of microlensing (from Table 1.) The microlensing distributions yield a mean magnification $\langle \mu \rangle$ that agrees with μ_0 to within numerical uncertainties.

saddle image near the lens galaxy in an asymmetric 2-image lens.

We do see the phenomenon that decreasing the fractional surface density in stars can increase the magnification dispersion, but only for the central image C, and — interestingly — only when the source is comparable to or smaller than the Einstein radius. Specifically, when $R_{\text{src}}/R_E = 1$ (middle panel of Figure 4), the magnification dispersion increases as f decreases all the way down to $f \approx 0.04$, and only then turns over. (The turnover is reassuring, because for $f \rightarrow 0$ there is no microlensing and the magnification dispersion must vanish.) When $R_{\text{src}}/R_E = 0.1$, the turnover happens at $f < 0.01$. By contrast, for a large source $R_{\text{src}}/R_E = 10$, the central image C follows the other images

in having a magnification dispersion that increases monotonically with f . While the behavior of image C at low f may have little practical importance, it is still useful for understanding how the magnification dispersion depends on the relative densities of stars and dark matter.

To make a final interpretation of Figure 4, it is useful to estimate an upper bound on the fractional surface density in stars at the position of each image. For PMN J1632–0033, Winn et al. (2003) show that the lens data are consistent with a total surface mass density of the form $\kappa_{\text{tot}} \propto R^{-\alpha}$ with $\alpha = 0.91 \pm 0.02$. They note that the lens galaxy is too faint to be characterized in detail with existing HST images, but appears to be an early-type galaxy with effective radius of $R_e \approx 0''.2$. To estimate the maximum possible stellar mass

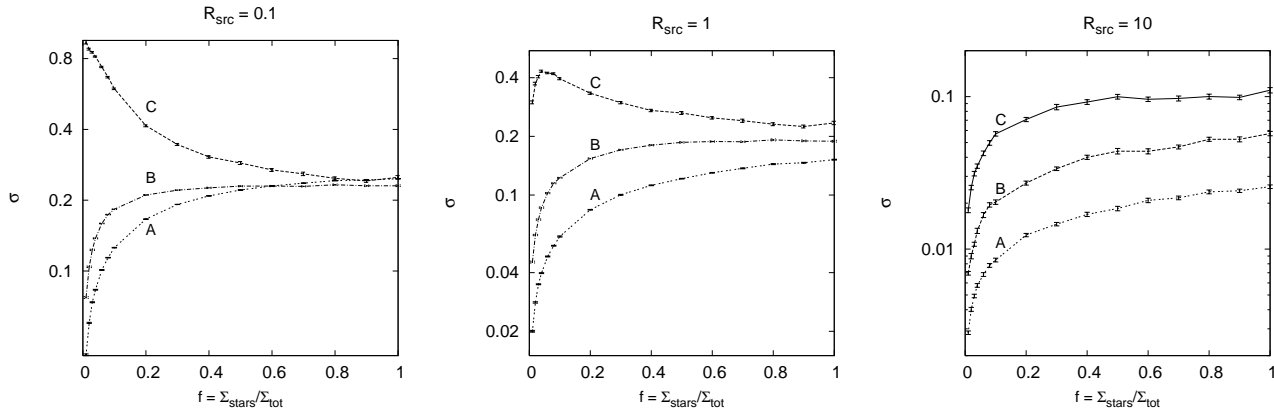


Figure 4. Magnification dispersion as a function of the fractional surface density in stars, $f = \kappa_{\text{stars}}/\kappa_{\text{tot}}$, for three different source sizes (quoted in units of R_E). The errorbars indicate the statistical uncertainties estimated with bootstrap and jackknife resampling (e.g., Efron 1982).

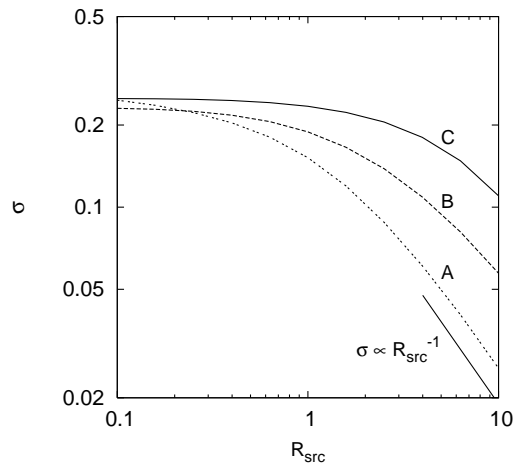


Figure 3. Magnification dispersion as a function of source size, for the three images, assuming $f = 100\%$ of the mass in stars. The line segment below the curve for image A shows the expected asymptotic scaling for large sources, $\sigma \propto R_{\text{src}}^{-1}$ (Refsdal & Stabell 1991, 1997).

density as a function of radius, we model κ_{stars} using a de Vaucouleurs $R^{1/4}$ law profile, and set the stellar mass-to-light ratio to the largest allowed value such that κ_{stars} never exceeds κ_{tot} . Using the observed radii of the three images ($R_A = 1''.38$, $R_B = 0''.09$, and $R_C = 0''.01$; see Winn et al. 2003), we obtain the f_{max} values listed in Table 2.

This analysis confirms our guess that the matter at image C could be essentially all stars. By contrast, the galaxy appears to be concentrated enough that at image B the density is no more than half stars, and at the distance corresponding to image A the density is no more than 1% stars. When we combine the upper limits on f with the σ versus f curves in Figure 4, we obtain the upper bounds on the magnification dispersion listed in Table 2. The bottom line is that microlensing is basically negligible for image A, but

Image	f_{max}	σ (in dex)		
		$R_{\text{src}} = 0.1$	1	10
A	0.013	0.05	0.02	0.003
B	0.511	0.23	0.19	0.04
C	0.997	0.25	0.23	0.11

Table 2. Column 2 gives our estimate of the upper limit on $f = \kappa_{\text{stars}}/\kappa_{\text{tot}}$ (see text). Columns 3–5 give upper limits on the magnification dispersion σ (in dex), for three source sizes (quoted in units of R_E). These upper limits were obtained by combining f_{max} with the σ vs. f curves in Figure 4. The dispersion can be extrapolated to larger source sizes with the scaling $\sigma \propto R_{\text{src}}^{-1}$ (Refsdal & Stabell 1991, 1997).

reasonably important for both images B and C. For large source sizes, the central image C is notably more affected by microlensing than the saddle image B, hence microlensing of such demagnified images can help reveal the source size.

4 DISCUSSION

Central lensed images, which are highly demagnified and naturally appear in places where the density of stars is high, are more susceptible to gravitational microlensing than the more familiar images that form at larger distances from lens galaxies. Therefore, it is useful to understand microlensing of central images in detail. We have performed numerical experiments to identify important aspects of the problem, and to raise some questions that warrant further theoretical attention.

The microlensing magnification maps for central (maximum) images differ qualitatively from those for familiar (minimum and saddle) images in striking ways. They do not show any of the classic fold and cusp caustic structures, but rather have concentrated blobs of high magnification amid large regions of demagnification. They also show notable inhomogeneity on scales of tens of Einstein radii. That structure causes microlensing fluctuations to be larger for

demagnified central images than for other images, even when the source is fairly large ($R_{\text{src}}/R_E \gtrsim 1$).

Our most intriguing qualitative result concerns the sensitivity of central image microlensing to the relative densities of stars and dark matter. When the source is large ($R_{\text{src}}/R_E \gtrsim 3$), the magnification dispersion decreases monotonically with the fraction f of density in stars. However, when the source is small ($R_{\text{src}}/R_E \lesssim 3$), the magnification dispersion *rises* as f is decreased from unity, reaches a peak at some finite value of f , and then falls to zero as $f \rightarrow 0$ (as it should in the absence of microlensing). This dependence is similar to behavior seen by Schechter & Wambsganss (2002) for a highly magnified saddle image. We do not see such behavior for a demagnified saddle, but we do see it for a demagnified central image. While this qualitative result has little practical importance (we expect $f \approx 1$ for central images), it may be valuable as insight into how microlensing depends on the relative amounts of stars and dark matter. If we can develop a full understanding of that problem, we may be able to turn microlensing into the best tool available for probing local *densities*, rather than integrated masses, of dark matter in distant galaxies (see Schechter & Wambsganss 2002, 2004).

One practical goal of microlensing studies is to probe the structure of the optical continuum emission regions at very high effective spatial resolution. The light curves produced by relative motion of the lens galaxy and source quasar can be used to map out the (1-dimensional) structure of the quasar on micro-arcsecond scales (Grieger et al. 1988, 1991; Agol & Krolik 1999; Mineshige & Yonehara 1999; Fluke & Webster 1999; Goicoechea et al. 2004). In terms of raw variability amplitude, it would seem that central images are the best targets for microlensing observations. Of course, there is the problem of detecting central images at optical wavelengths in the first place. A faint central image may be swamped by light from the lens galaxy. It may also be dimmed by extinction or scattering in the interstellar medium of the lens galaxy, although those effects might not be too much of a concern in the vast majority of lens galaxies that are ellipticals.

Our results allow us to consider how microlensing may affect various other applications that involve central lensed images. In PMN J1632–0033, the position and brightness of the central image lead to strong constraints on the density profile of the lens galaxy, and to upper limits on the mass of any supermassive black hole that may reside at the center of the lens galaxy (Winn et al. 2003, 2004). Those constraints are based on radio data, and at radio wavelengths the source is probably hundreds of stellar Einstein radii in size. While we have not explicitly considered such large sources, we can extrapolate our results using the scaling $\sigma \propto R_{\text{src}}^{-1}$ for large sources to infer that microlensing fluctuations at $R_{\text{src}}/R_E \sim 100$ are no more than a few percent. Even if they were as large as tens of percent, that would still be negligible compared with the orders of magnitude over which the magnifications of central images can vary due to modest changes in the smooth lens model (e.g., Keeton 2003). In other words, microlensing does not appear to be a significant concern for constraints on lens models drawn from radio observations of central images.

Perhaps even more interesting is the possibility that any central macro image produced by a lens galaxy containing

a supermassive black hole should be accompanied by a second, fainter central image (Mao et al. 2001; Bowman et al. 2004), and that the central image pair can be used to measure the black hole mass quite precisely (Rusin et al. 2004). The second central image would be a saddle rather than a maximum, so it would be interesting to consider whether a central saddle would have different microlensing properties than the central maximum we have considered. We suspect that, at the radio wavelengths where this application would be pursued, microlensing fluctuations are still small compared with changes in the smooth lens model. Nevertheless, it would be interesting to understand in detail how microlensing of central saddles compares with microlensing of central maxima.

We thank David Rusin and Josh Winn for interesting discussions, and for providing results from lens models of PMN J1632–0033.

REFERENCES

- Agol E., Krolik J., 1999, *ApJ*, 524, 49
 Bowman J. D., Hewitt J. N., Kiger J. R., 2004, *ApJ*, 617, 81
 Burke W. L., 1981, *ApJ*, 244, L1
 Chang K., Refsdal S., 1979, *Nature*, 282, 561
 Deguchi S., Watson W. D., 1987, *PRL*, 59, 2814
 Dyer C. C., Roeder R. C., 1980, *ApJ*, 238, L67
 Efron B., 1982, *The Jackknife, the Bootstrap, and Other Resampling Plans*. S.I.A.M., Philadelphia, PA
 Fluke C. J., Webster R. L., 1999, *MNRAS*, 302, 68
 Goicoechea L. J., Shalyapin V., Gonaález-Cadela J., Oscoz A., 2004, *A&A*, 425, 475
 Gott J. R., 1981, *ApJ*, 243, 140
 Granot J., Schechter P. L., Wambsganss J., 2003, *ApJ*, 583, 575
 Grieger B., Kayser R., Refsdal S., 1988, *A&A*, 194, 54
 Grieger B., Kayser R., Schramm T., 1991, *A&A*, 252, 508
 Inada N., et al., 2005, *astro-ph/0503310*
 Keeton C. R., 2003, *ApJ*, 582, 17
 Kochanek C. S., 2004, *ApJ*, 610, 69
 Lewis G. F., Irwin M. J., 1995, *MNRAS*, 276, 103
 Mao S., Witt H. J., Koopmans L. V. E., 2001, *MNRAS*, 323, 301
 Mineshige S., Yonehara A., 1999, *PASJ*, 51, 497
 Mortonson M. J., Schechter P. L., Wambsganss J., 2004, *astro-ph/0408195*
 Norbury M. A., Rusin D., Jackson N. J., Browne I. W. A., 2000, Abstracts from a conference held in Granada, 17-20 September 2000, and hosted by the Instituto de Radioastronomía Millimétrica (URAM), Universidad de Granada, and Instituto de Astrofísica de Andalucía (IAA)
 Pelt J., Schild R., Refsdal S., Stabell R., 1998, *A&A*, 336, 829
 Petters A. O., Levine H., Wambsganss J., 2001, *Singularity Theory and Gravitational Lensing*. Birkhäuser, Boston, MA
 Rauch K., Mao S., Wambsganss J., Paczyński B., 1992, *ApJ*, 386, 30
 Refsdal S., Stabell R., 1991, *A&A*, 250, 62
 Refsdal S., Stabell R., 1997, *A&A*, 325, 877

- Richards G. T., et al., 2004, *ApJ*, 610, 679
- Rusin D., Ma C.-P., 2001, *ApJ*, 549, L33
- Rusin D., Keeton C. R., Winn J. N., 2004, astro-ph/0412034
- Schechter P. L., Udalski A., Szymański M., Kubiak M., Pietrzyński G., Soszyński I., Woźniak P., Żebruń K., Szewczyk O., Wyrzykowski L., 2003, *ApJ*, 584, 657
- Schechter P. L., Wambsganss J., 2002, *ApJ*, 580, 685
- Schechter P. L., Wambsganss J., 2004, in *IAU Symposium No. 220*, eds. S. D. Ryder, D. J. Pisano, M. A. Walker, and K. C. Freeman (San Francisco: Astronomical Society of the Pacific), p. 103
- Schechter P. L., Wambsganss J., Lewis G. F., 2004, *ApJ*, 613, 77
- Schmidt R., Wambsganss J., 1998, *A&A*, 335, 379
- Schneider P., 1987, *ApJ*, 319, 9
- Schneider P., Ehlers J., Falco E. E., 1992, *Gravitational Lenses*. Springer, Berlin
- Wallington S., Narayan R., 1993, *ApJ*, 403, 517
- Wambsganss J., PhD Thesis (Munich 1990), also MPA report 550
- Wambsganss J., Paczyński B., Schneider P., 1990, *ApJ*, 358, L33
- Wambsganss J., 1992, *ApJ*, 386, 19
- Wambsganss J., 1999, *JCAM*, 109, 353-372
- Winn J. N., Rusin D., Kochanek C. S., 2003, *ApJ*, 587, 80
- Winn J. N., Rusin D., Kochanek C. S., 2004, *Nature*, 427, 613
- Woźniak P. R., Alard C., Udalski A., Szymański M., Kubiak M., Pietrzyński G., Żebruń K., 2000, *ApJ*, 529, 88
- Wyithe J. S. B., Webster R. L., Turner E. L., 2000, *MNRAS*, 315, 51
- Wyithe J. S. B., Turner E. L., 2001, *MNRAS*, 320, 21